



Hydrogen Tetrachloroaurate-Modulated PEDOT:PSS film assembled with conductive NPB buffer layer for High-Performance planar perovskite solar cells

Yansen Sun^{a,b,c}, Shuo Yang^d, Zhenyu Pang^{a,b,c}, Shaohua Chi^{a,b,c}, Xiaoxu Sun^{a,b,c}, Lin Fan^a, Fengyou Wang^a, Xiaoyan Liu^a, Maobin Wei^a, Lili Yang^{a,*}, Jinghai Yang^{a,*}

^a Key Laboratory of Functional Materials Physics and Chemistry of the Ministry of Education, Jilin Normal University, Changchun 130103, PR China

^b Changchun Institute of Optics, Fine Mechanics and Physics, Chinese Academy of Sciences, Changchun 130033, PR China

^c University of Chinese Academy of Sciences, Beijing 100049, PR China

^d College of Science, Changchun University, Changchun 130022, PR China

ARTICLE INFO

Keywords:

Optoelectronic properties
Localized surface plasmon resonance effects
Defect passivation
Charge transfer
Flexible devices

ABSTRACT

The further improvements in optoelectronic properties, hydrophobicity of poly(3,4-ethylenedioxythiophene):poly(styrenesulfonate) (PEDOT:PSS) hole transport layers, as well as regulation of defect states within devices are essential to promote the continued development of inverted p-i-n rigid and flexible planar perovskite solar cells (PSCs). However, the strong hygroscopicity, poor surface morphology, lower work function and coil configuration of pristine PEDOT:PSS films are detrimental to their own performance and growth dynamics process of perovskites, often resulting in severe energy losses and poor device performance. Herein, hydrogen tetrachloroaurate (III) hydrate (HAuCl₄·3H₂O) additive is combined with a conductive N,N'-Bis-(1-naphthalenyl)-N,N'-bis-phenyl-(1,1'-biphenyl)-4,4'-diamine (NPB) buffer layer to boost device performance by systematically modulating PEDOT:PSS and perovskite film. Wherein, the redox reaction between PEDOT:PSS and HAuCl₄ can cause phase segregation of PEDOT:PSS, improving the hydrophobicity, electrical conductivity, work function and surface morphology of the films. The reduced gold nanoparticles will produce localized surface plasmon resonance effects, thus enhancing the utilization of solar radiation by perovskite films. Furthermore, the suitable energy level alignment of NPB layer relative to perovskite and Au@PEDOT:PSS films will sufficiently exploit the dissociative excitons to facilitate effective hole transport, and the N atoms in NPB can also passivate defects at the interface by binding to uncoordinated Pb²⁺ ions, thereby reducing non-radiative open-circuit voltage loss and increasing short-circuit current density. A high power conversion efficiency (PCE) of 19.20% can be achieved for MA_{0.85}FA_{0.15}PbI₃ based p-i-n PSCs with negligible hysteresis and enhanced stability of devices. Similarly, the corresponding flexible device achieves a PCE of 14.04% with improved crumpling durability throughout low temperature preparation conditions below 140 °C. Our work presents a facile method to prepare high-efficient inverted PSCs while achieving improved long-term device stability.

1. Introduction

Organic-inorganic hybrid perovskite solar cells (PSCs) are experiencing an unprecedented period of rapid development in recent years. By virtue of the excellent optoelectronic performance of polycrystalline perovskites, the highest power conversion efficiency (PCE) of the PSCs so far has exceeded 25%, which can be comparable with that of commercial crystalline silicon solar cells. [1–3] Currently, inverted p-i-n planar-structured PSCs have attracted considerable attention and

manifested great potential for the exploitation in flexible devices and tandem solar cells due to their completely low-temperature preparation techniques and negligible hysteresis behavior. [4–6] Wherein, poly(3,4-ethylenedioxythiophene):poly(styrenesulfonate) (PEDOT:PSS) has become one of the most commonly used hole transport layers (HTLs) on account of its superior thermal stability, excellent solution processing and favorable mechanical flexibility, which is beneficial for its application in both rigid and flexible inverted photovoltaic (PV) devices. [7–9] However, p-i-n structured devices prepared by a one-step

* Corresponding authors.

E-mail addresses: lyang1980@126.com (L. Yang), jhyang1@jlnu.edu.cn (J. Yang).

<https://doi.org/10.1016/j.cej.2021.134358>

Received 22 August 2021; Received in revised form 21 December 2021; Accepted 22 December 2021

Available online 28 December 2021

1385-8947/© 2021 Elsevier B.V. All rights reserved.

antisolvent method generally suffer from poor PV performance compared with their n-i-p planar and mesoporous-based counterparts. It is largely due to the suboptimal optoelectronic performances of the PEDOT:PSS HTL. Such as, the electrical conductivity of pristine PEDOT:PSS films is rather low, usually less than 1 S cm^{-1} , and the mismatch of the valence band edge (VBE) between the HTL and the perovskite absorber layer, leading to a high energy barrier that suppresses the effective extraction of hole carriers. [10] In addition, the quality of the PEDOT:PSS films prepared by spin-coating method, especially for the flatness and uniformity, is also another key factor that affecting the crystal growth dynamics of polycrystalline perovskites and the PV performance of inverted planar PSCs. It has been proved that the poor quality of PEDOT:PSS films eventually leads to the formation of perovskite films with low crystallinity, inhomogeneous morphologies, smaller grain size and abundant grain boundaries. [11–13] All these will deteriorate the effective generation, separation and transport of photo-generated charge carriers within the devices, leading to severe open-circuit voltage (Voc) losses and relatively lower short-circuit current density (Jsc). [14] Even worse, the hydrophilic nature of PEDOT:PSS films and the poor quality of perovskite films will also have a negative impact on the long-term stability of PV devices. [15] Therefore, there is an urgent need to realize the synchronous regulation of the quality and optoelectronic properties of PEDOT:PSS and perovskite films.

So far, numerous strategies have been developed to regulate the quality and optoelectronic properties of PEDOT:PSS films, which can be divided into two main categories: co-mixing and post-treatment. [16–18] Where, it has been verified that the introduction of commonly used polar organic solvents, such as ethylene glycol (EG), dimethyl sulfoxide (DMSO) and diethylene glycol (DEG) into PEDOT:PSS aqueous solutions can improve the electrical conductivity of the films to a certain extent through dipole-charge interactions. [19–23] Nevertheless, the usage of the above polar solvents cannot effectively tune the work function and hydrophilicity of PEDOT:PSS films, which often results in PSCs with Voc less than 1 V and poor long-term stability. Moreover, methods such as acid (HCl, HNO₃, and H₂SO₄) post-treatment can also play a good regulatory role by inducing the phase segregation of PEDOT:PSS at the molecular level, where the positively charged H⁺ protons dissociated from the acids can bind to the negatively charged PSS⁻ parts to form the electrically neutral PSSH, and the hydrophilic part of PSSH can be dissociated from the PEDOT:PSS conjugated polymer system, which in turn can greatly enhance the electrical conductivity of the PEDOT:PSS films, while also improve the hydrophobic properties. [24] However, the above methods can more or less compromise the quality of the PEDOT:PSS films. On the other hand, in order to improve the quality of PEDOT:PSS films especially for flatness and uniformity, p-type materials such as PTAA and MoO_x have also been adopted to construct the double HTLs, which could allow for the better regulation of interface and also properly improve the quality of the polycrystalline perovskite films. [25,26] Nevertheless, there still remains an urgent need to develop and exploit some highly conductive materials to synergistically modulate the optoelectronic properties of perovskite films and their interfacial properties with HTLs. That is, it is invaluable to develop a practical and effective approach to enable the preparation of high-performance inverted p-i-n planar devices with negligible hysteresis and enhanced stability on both rigid and flexible substrates via systematically modulating the properties of PEDOT:PSS films.

In this work, we have combined additive doping with post-treatment methods to systematically modulate the PEDOT:PSS films to attain improved PV performance and stability of PSCs, which not only depends on the efficient transport and extraction of charge carriers, but also by taking full advantage of solar radiation and the favorable regulation of polycrystalline perovskite films. In detail, we initially introduced an appropriate amount of hydrogen tetrachloroaurate (III) hydrate (HAuCl₄·3H₂O) additive into the PEDOT:PSS aqueous solution, and then prepared the HAuCl₄-modified PEDOT:PSS HTLs using a low-temperature (140 °C) spin-coating method. The introduction of

HAuCl₄ is prospected to bring about the following effects. Firstly, it will enhance the electrical conductivity, hole mobility and work function of the PEDOT:PSS films due to the phase separation between the PEDOT chains and the PSS parts, accompanied by the conformational change of the PEDOT chains, which will further serve to ameliorate the balanced transport between holes and electrons. [27] Secondly, it is also promising to alter the hydrophilic/hydrophobic properties of the PEDOT:PSS substrates to some extent on account of the variations in the structure of PEDOT:PSS and the formation of Au nanoparticles (NPs), which contributes to improve the crystal growth dynamics process of polycrystalline perovskites and enhance the humidity stability of devices. Thirdly, the generation of Au NPs during the subsequent thermal annealing treatment will also bring about some benign effects, such as enhanced light absorption and exciton dissociation due to the localized surface plasmon resonance (LSPR) effects. Nevertheless, the presence of large amounts of Au NPs on the PEDOT:PSS films will increase the surface roughness of HTL, which impairs the effective extraction of hole carriers at the interface to some extent. [28] Therefore, to address this undesirable drawback, we prepared to subsequently spin-coat a p-type buffer layer of N,N'-bis-(1-naphthalenyl)-N,N'-bis-phenyl-(1,1'-biphenyl)-4,4'-diamine (NPB) with highly electrical conductivity on the HAuCl₄-doped PEDOT:PSS films. In particular, the hydrophobic and passivating effects of the NPB layers will help to regulate the crystal growth dynamics and interfacial properties of the perovskite films prepared on them, which further synergistically contributes to the improved PV performance and the long-term stability of the PSCs. Based on the above strategy and through a series of optimizations, we were able to achieve a champion PCE of 19.20% with a fill factor (FF) of 78.67%, Voc of 1.077 V and Jsc of 22.66 mA/cm² on the ITO rigid substrates, which is higher than that of 15.66% and 17.26% for the pristine and Au@PEDOT:PSS based devices, respectively. Given the excellent mechanical flexibility of PEDOT:PSS conjugated polymers, we have also further regulated the PV performance of the flexible PSCs based on the above optimization to further expand their diverse applications. Ultimately, all these improvements contributed to high-performance inverted flexible planar devices with the Voc value up to 0.942 V and a PCE of 14.04%. In addition, all these types of devices showed enhanced long-term stability and suppressed hysteresis behavior under ambient conditions. The substantial improvement in PV performance after the above modification can be attributed to the synergistic effects of the enhanced optoelectronic properties, quality, and work function of PEDOT:PSS films, improved quality and solar light absorption of perovskite films, the reduction of defect states within the devices, suppressed accumulation of interfacial charge carriers, and improved hydrophobicity.

2. Results and discussion

The favorable modification of PEDOT:PSS HTLs has shown great potential for boosting the PV performance of p-i-n planar PSCs, while also regulating the balanced transport of charge carriers and inhibiting the ion migration within polycrystalline perovskite films, which will further suppress the hysteresis behavior and enhance the stability of devices while synergistically regulating the Voc as well as Jsc of the devices. [29,30] To this end, we first introduced different amounts of inorganic HAuCl₄·3H₂O dopant into PEDOT:PSS aqueous solution and then assembled different concentrations of organic NPB buffer layers on top of it to systematically regulate the optoelectronic properties and film quality of the PEDOT:PSS films.

The optical absorption, transmission spectra and the corresponding dark current density–voltage (J-V) curves with the device architectures of ITO/(PEDOT:PSS/modified PEDOT:PSS)/Ag measured under the different modification conditions were shown in Figure S1, respectively. It can be seen from Figure S1a that the absorption intensity of the corresponding films gradually increases in the range of 350 nm to 500 nm accompanied by a broadened absorption peak as the doping

concentration of $\text{HAuCl}_4 \cdot 3\text{H}_2\text{O}$ increases from 20 mM to 60 mM, which can be attributed to the LSPR effect caused by Au NPs. [31] Similarly, we can see that the transmittance of the PEDOT:PSS films was slightly decreased in the range of 350 nm to 500 nm as presented in Figure S1b. Moreover, as shown in Figure S1c, we can find that the electrical conductivity reaches to the maximum when the doping concentration of HAuCl_4 is 40 mM. Therefore, the ultimate doping concentration of HAuCl_4 adopted in our work was 40 mM, and we then named the HAuCl_4 -modified PEDOT:PSS sample as Au@PEDOT:PSS, if not otherwise stated.

In order to systematically investigate the modulation effects of HAuCl_4 doping on PEDOT:PSS films, X-ray photoelectron spectroscopy (XPS) measurements were carried out. As can be seen from the XPS survey spectra presented in Fig. 1a, except for the signals from PEDOT:PSS, some extra peaks located around 84.21 eV, 87.91 eV, 335.91 eV and 354.25 eV can also be found in the Au@PEDOT:PSS film compared with the pristine one, which can be ascribed to the Au^0 signals. [32,33] Meanwhile, we presented the core-level spectra of Cl 2p, Au 4f, S 2p, O 1s, and N 1s signals of the pristine and modified PEDOT:PSS films, respectively. As shown in Fig. 1b and c, the presence of Cl 2p and Au 4f signals in Au@PEDOT:PSS film in comparison with the pristine one indicates that Au^{3+} ions in HAuCl_4 are reduced to Au NPs upon reaction with PEDOT:PSS, [34,35] which can enhance the absorption of incident solar radiation for perovskite films due to the LSPR effect. [36] The S 2p signals shown in Fig. 1d can be separated into two parts, 162 eV to 167 eV and 167 eV to 172 eV, which corresponds to the sulfur atoms in the PEDOT thiophene ring and the PSS^- unit, respectively. Each sulfur peak presents a double-peak format caused by the spin splitting effect. Subsequently, we split the various species of S 2p peaks in the above samples with performing Gauss-Lorentz fitting on their spectra. The detailed parameters can be found in Table S1. [37] It can be found that both S $2p_{1/2}$ and S $2p_{3/2}$ signals of Au@PEDOT:PSS films are shifted toward higher binding energies compared with those in the pristine ones. According to previous reports, the introduction of HAuCl_4 into PEDOT:PSS aqueous solutions can lead to phase segregation of the positively

charged PEDOT and negatively charged PSS portions, because the H^+ dissociated from HAuCl_4 in the solution can bind to the insulating PSS^- to form the electrically neutral PSSH. Meanwhile, the above reaction also leads to the PEDOT chains being surrounded by some AuCl_4^- anions in the solution. The larger shift in the S signals of the PSS^- portion indicates a reduction in the negative charge of the PSS chain due to the formation of neutral PSSH. [38] Such change can alter the conformation of the PEDOT chain from a coil structure to a linear or extended-coil structure, which leads to the enhancement of the electrical conductivity of PEDOT:PSS films. [39,40] Moreover, we further calculated the intensity ratio of the PEDOT to PSS part, where a larger ratio of 0.31 could be obtained for the Au@PEDOT:PSS sample. The higher ratio compared with that of 0.24 for the pristine one further verifies the phase separation of the films and is coincided with the enhanced electrical conductivity behavior described above. Since both the PEDOT and PSS^- units contain O atoms as well, we then analyzed the peak shift of the O 1s fine scan and performed the Gauss-Lorentz fit to them, as shown in Fig. 1e and Table S2. Similarly, for the Au@PEDOT:PSS film, the O 1s peak near 532 eV of the PSS^- part also exhibits a shift toward large binding energy and a concomitant decrease in the ratio of S = O associated with the PSS portion, which well confirms the above discussion about the reduction of the PSS chain due to phase separation of PEDOT:PSS.

Fig. 2 showed the Raman spectra in the range of 200 cm^{-1} to 1800 cm^{-1} to further testify the regulatory mechanism of HAuCl_4 doping on PEDOT:PSS films. As shown in Fig. 2a, the Au@PEDOT:PSS film exhibits relatively stronger peaks, which are mainly attributed to the enhanced light scattering ability of Au NPs resulting from the local field enhancement of the dipole resonance peaks. [41] As shown in Fig. 2b, all the films present a strong characteristic peak near 1440 cm^{-1} , which corresponds to the symmetric stretching vibrations of $\text{C}_\alpha = \text{C}_\beta$, while the asymmetric $\text{C}_\alpha = \text{C}_\beta$ vibrations related to the middle and thiophene rings of the chains are located at 1505 cm^{-1} and 1572 cm^{-1} , respectively. In addition, the other Raman peaks at 1369 cm^{-1} and 1537 cm^{-1} are associated with the stretching of $\text{C}_\beta\text{-C}_\beta$ and the splitting of the

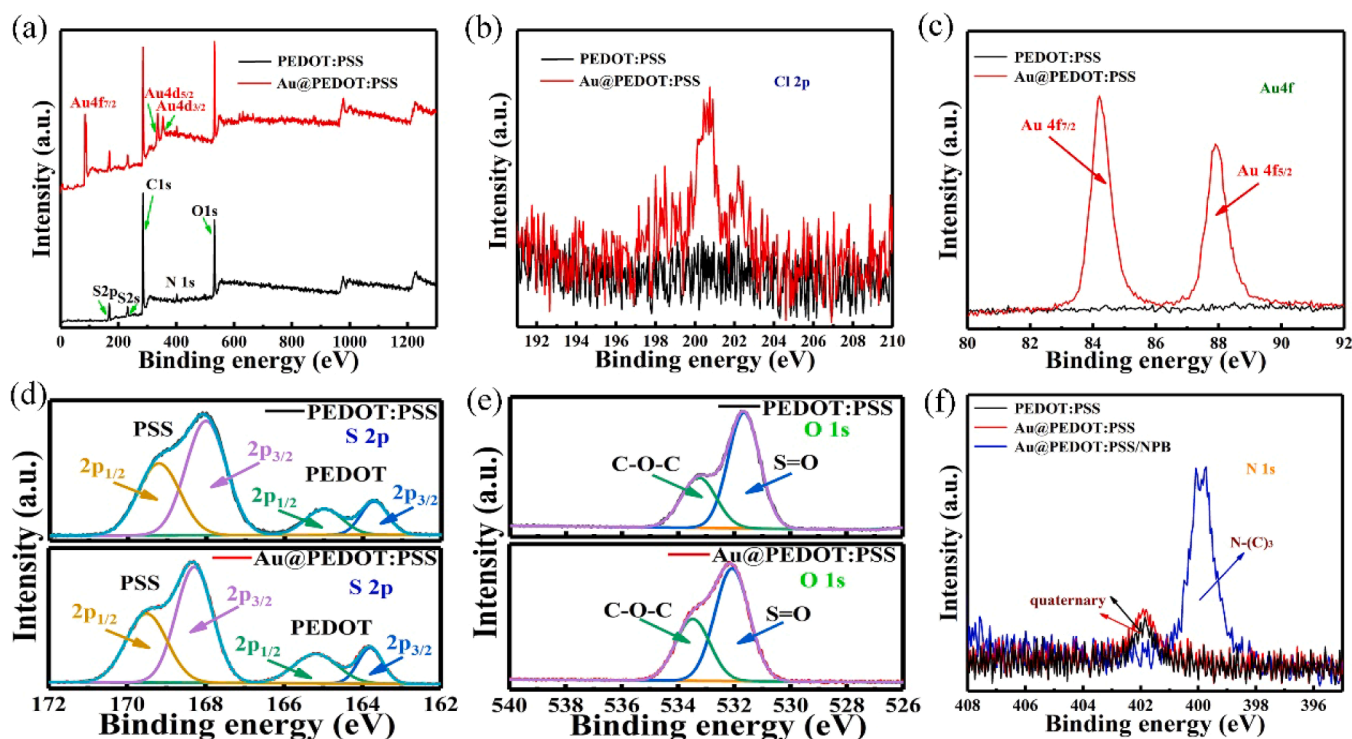


Fig. 1. XPS spectra of pristine, Au@PEDOT:PSS and Au@PEDOT:PSS/NPB (4 mg/ml) films of (a) Survey spectra, (b) Cl 2p, (c) Au 4f, (d) S 2p, (e) O 1s, (f) N 1s core-level spectra.

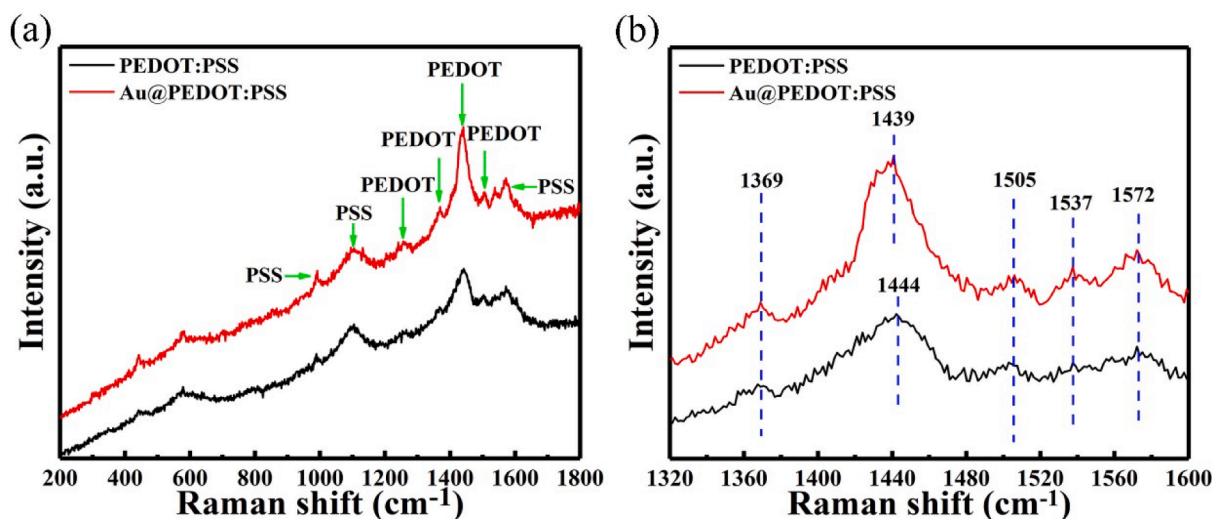


Fig. 2. Raman spectra of pristine, Au@PEDOT:PSS films for (a) full spectra, (b) enlarged spectra in the range of 1320 cm^{-1} and 1600 cm^{-1} .

asymmetric $C_{\alpha} = C_{\beta}$ vibrations, respectively. [42,43] The blue shift of the main characteristic Raman peaks in Au@PEDOT:PSS film in comparison with that in the pristine one is associated with the variations in the neutral, oxidized structures and conformation of the PEDOT chains, which indicates that more oxidation states will be generated in Au@PEDOT:PSS films after the neutral benzoid PEDOT is changed into the polaritons (radical cations) and bipolaritons (bication) quinoid structures. [44] The specific reaction mechanism is stated as follows: where, the H^{+} protons dissociated by HAuCl_4 in PEDOT:PSS aqueous solution can combine with the SO_3^{-} groups of the PSS part to form the electrically neutral PSSH, which in turn reduces the coulombic interaction between PSS and PEDOT, leading to the phase separation of PEDOT:PSS. The above reaction can be described as $\text{HAuCl}_4 + \text{PSS}^{-} \rightarrow \text{PSSH} + \text{AuCl}_4^{-}$. Meanwhile, the redox reaction between AuCl_4^{-} and PEDOT will also occur, resulting in the conformational change of PEDOT chains from the neutral benzoid to the polaritons (radical cations) and bipolaritons (bication) quinoid structures, which is consistent with the analysis results of Raman as well as XPS measurements. As a result, Au^{3+} can be reduced to Au^0 during this process, and the S atom in the PEDOT leads to the destruction of the aromatic structure after the loss of electrons, and the resulting cation reduces the energy by forming a quinone structure, which in turn leads to the production of polaritons and bipolaritons in PEDOT. [45–47] The schematic chemical diagrams of the different structures of PEDOT were presented in Figure S2 to more intuitively understand the mechanism of the generation of more oxidation states in the PEDOT chains. Such results are in good agreement with the above XPS analysis.

The phase separation of the PEDOT and PSS portions caused by HAuCl_4 doping is a key factor in enhancing the mobility of charge carriers and the electrical conductivity of the films, thus enhancing the extraction capability of hole carriers. Herein, Raman scattering technique is an effective means to deeply investigate the changes of the above vibration modes of chemical bonds with different structures. Therefore, we further characterized the PEDOT:PSS films doped with different concentrations of HAuCl_4 additives using Raman measurements and processed a Gauss-Lorentz fitting on the main peaks. It can be seen that the main peak near 1443 cm^{-1} can be divided into two peaks around 1421 cm^{-1} and 1446 cm^{-1} , which corresponds to the quinoid polarized and neutral benzoid structures of PEDOT chains, respectively, as shown in Figure S3. [48] Meanwhile, the degree of oxidation of the PEDOT chains can be determined by the intensity ratio of $I_{\text{polaron}}/I_{\text{neutral}}$, which has been summarized in Table S3. It can be seen that as the doping amount of HAuCl_4 increases from 10 mM to 40 mM, the $I_{\text{polaron}}/I_{\text{neutral}}$ in the PEDOT chain gradually increases from 0.54 to 0.64 and 0.75

compared with the pristine one. The enhanced polaron content is consistent with the trend of gradual improvement in electrical conductivity presented in Figure S1c. However, with the doping amount of HAuCl_4 further reaches to 60 mM, the $I_{\text{polaron}}/I_{\text{neutral}}$ was dropped to 0.69, which means that the excessive concentration of HAuCl_4 inhibits the further enhancement of conductivity of Au@PEDOT:PSS film. [49] Of course, it may also ultimately affect the energy band structure of the pristine PEDOT:PSS films, which will be discussed in the following sections.

Even so, the existence of Au NPs will also be detrimental to the subsequent preparation of high-quality perovskite films and affect their interfacial properties to some extent. In particular, when the doping amount of HAuCl_4 reaches saturated, excessive Au NPs will accumulate on the surface of the PEDOT:PSS films, which will severely impair the uniformity and flatness of the PEDOT:PSS films, and lead to the decrease of the electrical conductivity. [50] To overcome the above-mentioned problems, we post-treated the Au@PEDOT:PSS films with NPB under the condition of moderate amount of Au NPs.

To determine the optimum concentration of NPB for use on Au@PEDOT:PSS films, Au@PEDOT:PSS HTLs modified with 2 mg/ml, 4 mg/ml and 6 mg/ml of NPB were prepared, and a series of characterizations were carried out. Now, let's pay back attention to Figure S1a and b that the assembly of the NPB buffer layer enables the down-conversion of UV light, which contributes to improve the light stability of the devices. [51] Meanwhile, the electrical conductivity of the modified PEDOT:PSS films will reach the maximum when the concentration of NPB is 4 mg/ml, as presented in Figure S1b. After calculation, the specific values of the electrical conductivity of pristine, 20 mM to 60 mM Au@PEDOT:PSS, and 40 mM Au@PEDOT:PSS/NPB (2 mg/ml to 6 mg/ml) HTLs are $6.27 \times 10^{-4}\text{ mS cm}^{-1}$, $7.59 \times 10^{-4}\text{ mS cm}^{-1}$, $9.66 \times 10^{-4}\text{ mS cm}^{-1}$, $8.59 \times 10^{-4}\text{ mS cm}^{-1}$, $1.03 \times 10^{-3}\text{ mS cm}^{-1}$, $1.25 \times 10^{-3}\text{ mS cm}^{-1}$ and $1.13 \times 10^{-3}\text{ mS cm}^{-1}$, respectively.

To unveil the effect of NPB in Au@PEDOT:PSS/NPB (4 mg/ml) film on the above enhanced optical and electronic properties, X-ray diffraction (XRD), scanning electron microscope (SEM) and energy dispersive X-ray spectroscopy (EDS) were further carried out to investigate the variations of phase structure, morphology and composition. As shown in Figure S4, the as-prepared PEDOT:PSS HTLs exhibit amorphous features, where the diffraction peaks at 30.1° , 35.1° and 50.3° correspond to the (222), (400) and (440) crystal planes of the ITO substrate, respectively. By comparison, some other typical characteristic diffraction peaks of Au@PEDOT:PSS and Au@PEDOT:PSS/NPB (4 mg/ml) films at 38.1° and 44.7° were also observed, which can be attributed to the (111) and (200) crystal planes of the generated Au NPs,

respectively. [52,53] Moreover, a diffraction peak around 10° was observed in the XRD pattern of the Au@PEDOT:PSS/NPB (4 mg/ml) film, which can be ascribed to the (1 0 1) plane of the NPB buffer layer and well indicates the formation of NPB films. [54] As can be seen from the N 1s XPS spectra in Fig. 1f, the strongest N 1s signal of 398.6 eV appears in Au@PEDOT:PSS/NPB (4 mg/ml) film, which can be assigned to the highly symmetric N-(C)₃ form. It is necessary to point out that the signal located near 401.8 eV (quaternary form) in both pristine and Au@PEDOT:PSS samples can be attributed to some additions, such as positively charged amino groups in PEDOT:PSS aqueous solutions. [55] These results prove that NPB has been successfully covered on Au@PEDOT:PSS films. SEM and EDS images presented in Figure S5 and S6 indicate that all the films exhibit a high degree of homogeneity and continuity. The presence of some uniformly sized and discrete Au NPs in all modified PEDOT:PSS films suggests that the usage of NPB does not induce agglomeration of the produced Au NPs and thus will not further deteriorate the interfacial properties of the devices. To further characterize the size of the Au NPs generated on the films, TEM measurements were performed on 40 mM Au@PEDOT:PSS sample, as shown in Figure S7. We can see that from the high resolution transmission electron (HRTEM) images the average size of the Au NPs can be determined to be about 10 nm. It can be seen from the selected area electron diffraction (SAED) images as well as the fast Fourier transform (FFT) analysis that the lattice spacing is 0.23 nm, which corresponds to the (1 1 1) plane of Au. [56] In short, considering the down-conversion effect of NPB on UV light and its high conductivity, Au@PEDOT:PSS/NPB (4 mg/ml) substrate will not only generate more charge carriers, but also enhance the absorption of perovskite films from 350 nm to 550 nm, which is beneficial to the improvement of the PV performances of the devices. [51]

Considering that the surface morphology and roughness of the films are thought to be one of the key factors affecting the optoelectronic performances of the HTLs and the extraction properties of the interfacial charge carriers of the p-i-n devices, we then performed atomic force microscopy (AFM) measurements on both pristine and these modified PEDOT:PSS films. As shown in Fig. 3, the root mean square (RMS)

roughness of pristine, Au@PEDOT:PSS and Au@PEDOT:PSS HTLs post-treated with 2 mg/ml, 4 mg/ml and 6 mg/ml of NPB were 8.42 nm, 9.17 nm, 8.11 nm, 7.72 nm and 7.24 nm, respectively. Such reduced RMS would provide a desired platform for the growth of perovskite films. [57] Meanwhile, we also provided the AFM phase images of the above HTLs, as presented in Figure S8. It can be seen that the AFM phase images of these films exhibit different formats before and after the usage of HAuCl₄ doping as well as NPB post-treatment. According to previous work, we have learnt that for the pristine PEDOT:PSS films, the conductivity-rich PEDOT portion and the insulation-rich PSS portion are uniformly distributed throughout the film, which is consistent with the light and dark characteristics of the film grains in phase image presented in Figure S8a. [58] Moreover, when PEDOT:PSS film undergoes phase separation, the conductive PEDOT:PSS bright regions will show more fibrous structure, which is consistent with the results in Figure S8b-e. [59] Therefore, this further verifies that the introduction of HAuCl₄ in PEDOT:PSS aqueous solution can induce phase separation of the PEDOT:PSS films. We have also conducted the contact angle measurement on the corresponding HTLs using perovskite precursor solutions. As presented in Figure S9, the contact angle gradually increases from 14.1° to 42.4° , 64.8° , 67.3° and 69.9° . Where the enhanced hydrophobicity of Au@PEDOT:PSS film compared with the pristine PEDOT:PSS films can be attributed to the synergistic regulation of the change in work function, the increase in PEDOT/PSS ratio and the increase in surface roughness of the films. Moreover, the introduction of the NPB buffer layer can further enhance the hydrophobicity since it contains many rigid phenyl groups, which is beneficial to the reduction of the nucleation density of the perovskite crystals, the increase of the grain size, and ultimately improves the humidity stability of the devices. [60]

The crystal quality of perovskite films on these HTLs was further characterized by XRD measurements. As shown in Figure S10a, all the films exhibit a tetragonal structure with the main diffraction peaks located at 14.1° , 28.4° and 32° , corresponding to the crystal planes of (1 1 0), (2 2 0) and (3 1 0), respectively. Compared with that of the pristine film, a gradual increase in the relative diffraction intensity appeared of the perovskite films deposited on both Au@PEDOT:PSS and

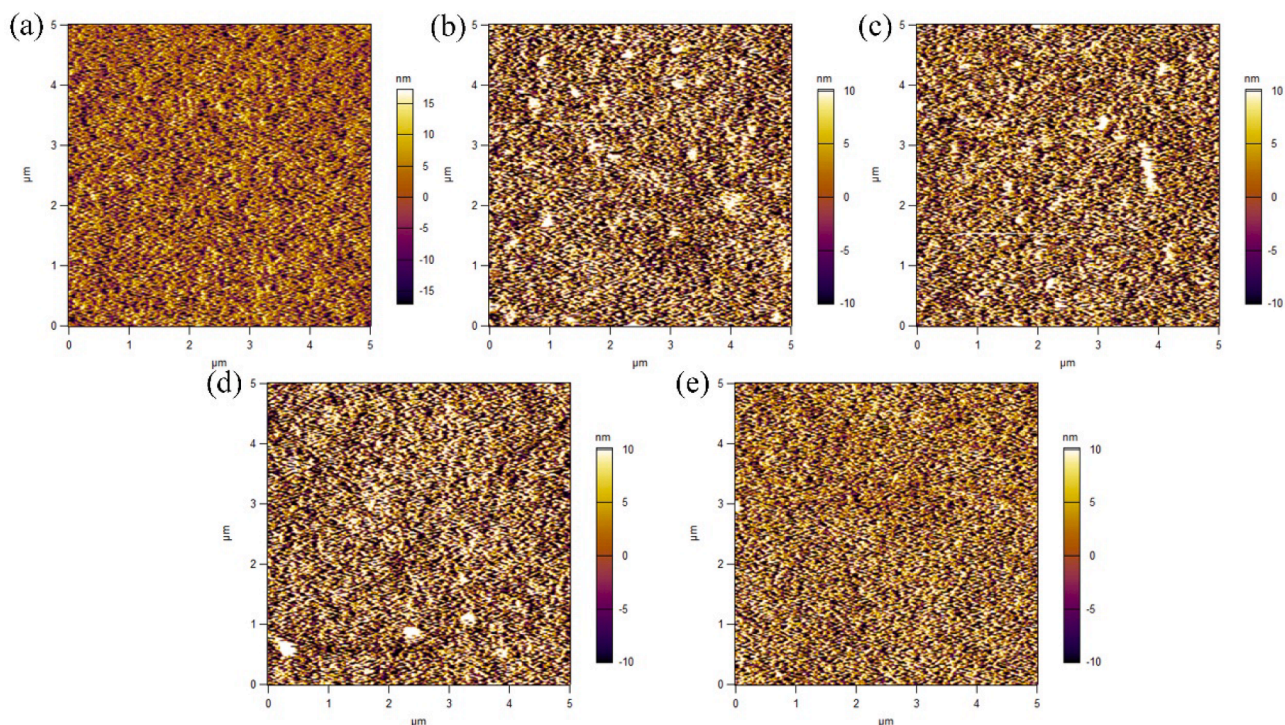


Fig. 3. AFM images of (a) pristine, (b) Au@PEDOT:PSS, (c) Au@PEDOT:PSS/NPB (2 mg/ml), (d) Au@PEDOT:PSS/NPB (4 mg/ml), (e) Au@PEDOT:PSS/NPB (6 mg/ml) HTLs.

Au@PEDOT:PSS HTLs modified with different concentrations of NPB, indicating an increase in crystallinity. Moreover, all the films have an extra diffraction peak at 12.6° , which could be attributed to the unreacted PbI_2 . [61] It is known from the previous work of You et al. that the presence of moderate amounts of PbI_2 will play a positive effect on the passivation of defects on the surface and at grain boundaries of the perovskite films. [62] Meanwhile, the usage of NPB can lead to a decrease in the peak intensity of PbI_2 due to the passivating effect of NPB, which is due to the ability to bind to the uncoordinated Pb^{2+} ions, thus retarding the crystallization rate of perovskites and improving the film-forming quality of perovskite films. To more visually present this phenomenon, we summarized the relative intensities of the diffraction peaks of the different crystalline planes for the above films, as shown in Table S4, and it can be seen that the trend of the variation of the diffraction peak intensities is consistent with the results we discussed above. The UV–vis absorption spectra of the perovskite films deposited on these HTLs were also presented in Figure S10b, and the trend of the enhanced absorption intensity of the perovskite films deposited on these modified HTLs also exhibited the same variation rule as that in the XRD patterns. That is, the optimum modification effect will be achieved when the concentration of NPB is 4 mg/ml. Apparently, the introduction of an appropriate thickness of NPB buffer layer on Au@PEDOT:PSS films can successfully modulate the crystal growth dynamics of polycrystalline perovskites and their interfacial properties, thus resulting in an improvement in the quality of perovskite films and ultimately leading to the enhanced absorption ability of solar radiation. Also, since the solvents DMF and DMSO cannot dissolve the NPB buffer layer, the N atoms containing lone pairs of electrons in the NPB molecule are allowed to bind to the uncoordinated Pb^{2+} ions according to the Lewis acid-base theory.

To investigate whether there are coordination interactions between NPB and PbI_2 occur, we have successively performed the crystal growth dynamics, FTIR, and XPS measurements on perovskite films, respectively. Firstly, we investigated the interaction between NPB and PbI_2 from a macroscopic perspective by recording the color change of polycrystalline perovskite films spin-coated on PEDOT:PSS and PEDOT:PSS/NPB substrates at different periods. It can be seen from Figure S11 that the crystallization process of the perovskite films on PEDOT:PSS/NPB substrate is significantly retarded compared with those prepared on the PEDOT:PSS film. From the FTIR spectra of perovskite films prepared on

PEDOT:PSS and PEDOT:PSS/NPB films, we can see that the N–H ($\nu(\text{N–H})$) stretching vibration undergoes a red shift from 3115.95 cm^{-1} to 3121.49 cm^{-1} . Meanwhile, the N–H ($\nu(\text{N–H})$) bending vibration is also shifted from 1461.34 cm^{-1} to 1463.63 cm^{-1} . As shown in Figure S12a–c. [63] Furthermore, it is also evident from the core-level XPS spectra of the Pb 4f and I 3d signals presented in Figure S12d–e that the binding energies of both Pb and I signals of the NPB-modified perovskite films prepared on PEDOT:PSS substrates are shifted toward lower binding energies compared with those of pristine perovskite films prepared on PEDOT:PSS substrates. According to previous work, we have learnt that the coordination reactions between Pb^{2+} ions and N atoms in the molecules can lead to shifts in the wave number of bond vibrations and peak binding energies of perovskite films, which is consistent with the phenomena in our case. [64,65] Thus, it is reasonable to believe that the nonradiative recombination of photogenerated carriers can be effectively suppressed in polycrystalline perovskite films and their interfaces.

To further investigate the effect of the above optimization on the surface morphology of the perovskite films, top-view SEM images of the perovskite films prepared on these HTLs are also presented in Fig. 4, and the corresponding statistical grain size distribution of these films is also provided in Figure S13. Where, the perovskite films prepared on the pristine PEDOT:PSS HTL exhibited the smallest grain size, the least uniform grain distribution and the worst surface morphology. Such phenomena were moderately improved in both Au@PEDOT:PSS and Au@PEDOT:PSS HTLs post-treated with different concentrations of NPB. The cross-sectional SEM images presented in Figure S14 also show well-crystallized perovskite films with larger grain size and improved interfacial properties, i.e., an obvious well-defined interfacial hierarchy can be found in both Au@PEDOT:PSS and the above NPB post-treated Au@PEDOT:PSS samples, especially when the concentration of NPB used is 4 mg/ml. We further conducted AFM measurements on perovskite films deposited on pristine, Au@PEDOT:PSS and Au@PEDOT:PSS HTLs post-treated with different concentrations of NPB. As illustrated in Figure S15, we can see the reduction of RMS roughness from 10.85 nm to 9.81 nm, 9.47 nm, 7.87 nm and 8.32 nm, respectively. All the above characterizations emphasize the importance of introducing π -conjugated conductive NPB buffer layers on Au@PEDOT:PSS films for further interfacial modifications. Such reduction of grain boundaries and improvement of interfacial properties will play a positive role in the

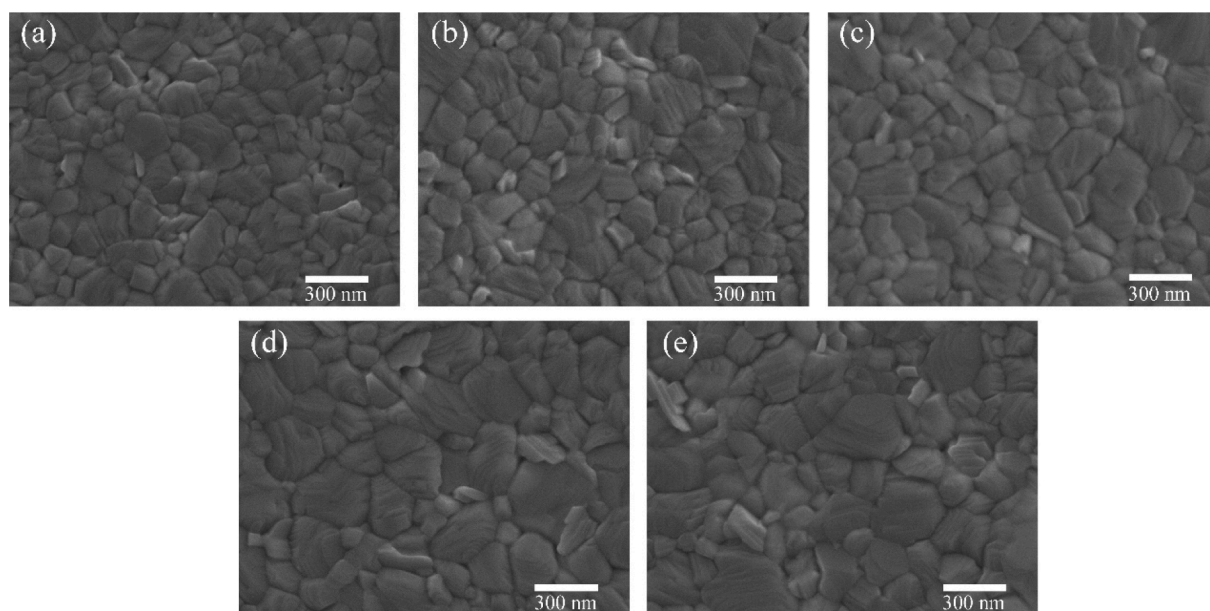


Fig. 4. SEM images of $\text{MA}_{0.85}\text{FA}_{0.15}\text{PbI}_3$ -based perovskite films spin-coated on (a) pristine, (b) Au@PEDOT:PSS, (c) Au@PEDOT:PSS/NPB (2 mg/ml), (d) Au@PEDOT:PSS/NPB (4 mg/ml), (e) Au@PEDOT:PSS/NPB (6 mg/ml) HTLs.

passivation of defects, modulation of charge carrier transport as well as improvement of device stability. [66] This will not only help to effectively separate the excitons generated by perovskite and Au NPs, but also further improve the interfacial contact at the perovskite/HTL interface to reduce the leakage current losses and improve the PV performance of the devices.

Based on the above analysis, 4 mg/ml was finally determined as the optimum concentration of NPB in our case, which helped to form a thin buffer layer with a thickness of about 10 nm. Then, we named the HTLs co-modified with HAuCl_4 and NPB as Au@PEDOT:PSS/NPB samples. Thereafter, we constructed PSCs with optimized Au@PEDOT:PSS/NPB HTLs on both rigid and flexible substrates. To further characterize the device performance, current density–voltage (J-V) measurements were performed on devices with the structures of glass/ITO/HTL/ $\text{MA}_{0.85}\text{FA}_{0.15}\text{PbI}_3/\text{PC}_{61}\text{BM}/\text{BCP}/\text{Ag}$. The usage of BCP can suppress the accumulation of electrons at the interface and create an ohmic contact between the ETL and Ag electrodes, which has been shown to help further improve the FF of the devices. [67] Details of the J-V characteristic curves and PV parameters during device optimization can be found in Figure S16 and Table S5. The highest power conversion efficiencies (PCEs) can be obtained under reverse scan (RS) conditions when the concentration of NPB adopted is up to 4 mg/ml, and part of the PV parameters start to decrease with the further increase in NPB concentration.

The forward scan (FS) and RS J-V curves for all pristine, Au@PEDOT:PSS and Au@PEDOT:PSS/NPB based champion PSCs are shown in Fig. 5a and Table 1 along with the detailed parameters. Wherein, the PCEs of the pristine PSC under RS and FS conditions were 15.66% and 14.22%, respectively. While, the corresponding PCEs of Au@PEDOT:PSS and Au@PEDOT:PSS/NPB based PSCs under RS and FS conditions were 17.26%, 16.34%, and 19.20%, 18.43%, respectively. The external quantum efficiency (EQE) spectra of these devices were shown in Fig. 5b. The integrated Jsc values of the corresponding devices can be derived to be 19.27 mA/cm^2 , 20.29 mA/cm^2 and 21.41 mA/cm^2 ,

Table 1

PV parameters of pristine, Au@PEDOT:PSS, and Au@PEDOT:PSS/NPB based champion PSCs measured under different scan directions.

Device	Direction	Jsc (mA/cm^2)	Voc (mV)	FF (%)	PCE (%)
Pristine	RS	21.13	1004	73.84	15.66
	FS	20.67	994	69.19	14.22
Au@PEDOT:PSS	RS	21.91	1048	75.17	17.26
	FS	21.68	1044	72.21	16.34
Au@PEDOT:PSS/NPB	RS	22.66	1077	78.67	19.20
	FS	22.51	1073	76.31	18.43

respectively, which were well matched with the trends of the J-V curves. Then, we calculated the hysteresis index (HI) to quantify the hysteresis behavior of these champion devices, where the formula is shown as below: [68]

$$\text{HI} = (\text{PCE}_{\text{reverse}} - \text{PCE}_{\text{forward}}) / \text{PCE}_{\text{reverse}}$$

The HI of the pristine PSC was 0.092, while it was reduced to 0.053 and 0.040 for Au@PEDOT:PSS and Au@PEDOT:PSS/NPB based ones, respectively. Obviously, Au@PEDOT:PSS/NPB based PSC exhibited the best PV performance, which can be attributed to the moderate improvements in Jsc, Voc and FF compared with those of the pristine one. Based on the above discussion about HTLs and perovskite films, it is reasonable to believe that all the above-mentioned improvements in the performance of Au@PEDOT:PSS/NPB based devices can be ascribed to the enhanced electrical conductivity of HTLs, the improved quality of perovskite films, the enhanced light absorption due to the LSPR effect of Au NPs, and the positive role of NPB in passivating the uncoordinated Pb^{2+} -induced defects within the perovskite films and at the interface.

To comprehensive quantify the defect density within the perovskite film and at the interface with the HTL, space-charge limited current (SCLC) measurements were performed on hole-only device structure of ITO/HTL/perovskite/Spiro-OMeTAD/Ag. As shown in Fig. 5c, we evaluated the trap density (N_t) using the formula $N_t = 2V_{\text{TFL}}\epsilon\epsilon_0/eL^2$,

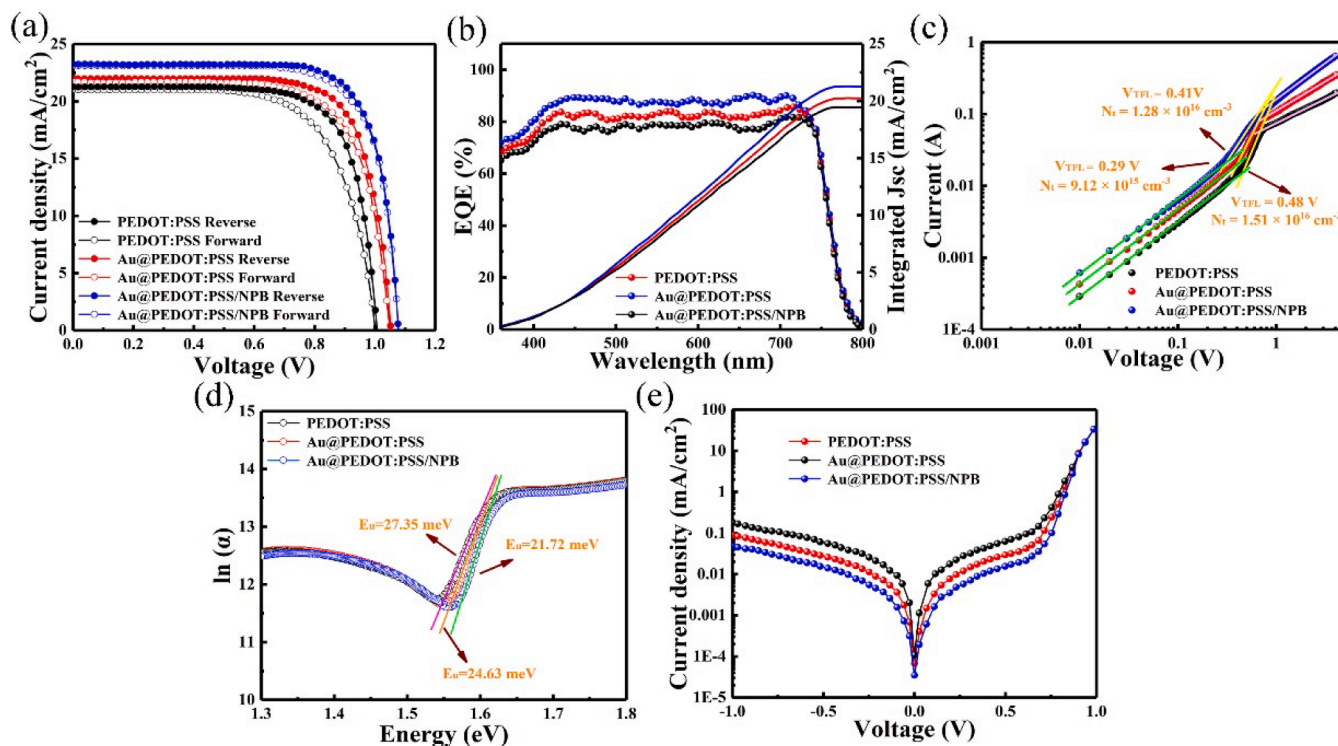


Fig. 5. (a) Champion J-V curves of pristine, Au@PEDOT:PSS, and Au@PEDOT:PSS/NPB based PSCs measured under RS and FS directions. (b) The corresponding EQE spectra of these champion devices. (c) SCLC spectra of the corresponding hole-only devices. (d) Urbach energy of perovskite films on pristine, Au@PEDOT:PSS, and Au@PEDOT:PSS/NPB HTLs. (e) Dark J-V characteristic curves of the corresponding devices.

where V_{TFL} is the trap-filled limit voltage, ϵ is the dielectric constant of $MA_{0.85}FA_{0.15}PbI_3$ -based perovskite film (32), ϵ_0 is the vacuum permittivity ($8.854 \times 10^{-14} \text{F/cm}$), e is the elemental charge ($1.6 \times 10^{-19} \text{C}$), and L is the thickness of perovskite film (350 nm). [69,70] After calculation, the Au@PEDOT:PSS/NPB sample presented a lower N_t of $9.12 \times 10^{15} \text{cm}^{-3}$ compared with that of the pristine ($1.51 \times 10^{16} \text{cm}^{-3}$) and Au@PEDOT:PSS ($1.28 \times 10^{16} \text{cm}^{-3}$) based ones, indicating that the trap states have been effectively passivated by the co-modification of HAuCl_4 and NPB due to the improved quality of HTLs, perovskite films as well as the interfacial properties. Moreover, we have also calculated the Urbach energy (E_u) of perovskite films spin-coated on the pristine, Au@PEDOT:PSS and Au@PEDOT:PSS/NPB HTLs to investigate the variation of defect state densities within the devices. [71] As shown in Fig. 5d, the E_u value of the perovskite film on Au@PEDOT:PSS/NPB HTL was 21.72 meV, which was smaller than that on the pristine (27.35 meV) and Au@PEDOT:PSS (24.63 meV) based HTLs, further indicating the suppression of unfavorable defects by the above co-modification technique. To further verify the improvement in interfacial properties within the devices, dark J-V measurements were also performed, as shown in Fig. 5e. A smaller dark current density can be found in the Au@PEDOT:PSS/NPB based device, which further indicated that the optimization of the interfacial contacts inhibits the charge carrier recombination

process. In turn, led to relatively low current leakage, which was also beneficial to the enhancement of V_{oc} and FF in PV devices. Clearly, both the fewer defects within the Au@PEDOT:PSS/NPB based perovskite films and the corresponding better interfacial properties point to good performance of charge behaviors.

Thus, we subsequently conducted steady-state photoluminescence (PL) and time-resolved photoluminescence (TRPL) measurements on perovskite films spin-coated on pristine, Au@PEDOT:PSS and Au@PEDOT:PSS/NPB HTLs to systematically elucidate the dynamics processes changes in charge carrier extraction and recombination, respectively. As shown in Fig. 6a, progressively enhanced PL quenching effects can be found of perovskite films spin-coated on pristine, Au@PEDOT:PSS and Au@PEDOT:PSS/NPB HTLs relative to that on the glass substrate. Moreover, all the TRPL curves were presented in Fig. 6b and fitted by using the bi-exponential decay function $I(t) = A_1 \exp(-t/\tau_1) + A_2 \exp(-t/\tau_2)$. [72] For the perovskite films spin-coated on glass, pristine, Au@PEDOT:PSS and Au@PEDOT:PSS/NPB HTLs, the corresponding average lifetimes decreased from 33.94 ns to 10.20 ns, 6.67 ns and 4.43 ns, respectively, where the detailed parameters can be seen in Table S6. We also conducted transient photovoltage (TPV) measurements to further explore and validate the changes in charge transport and recombination dynamics processes of perovskite films on the pristine,

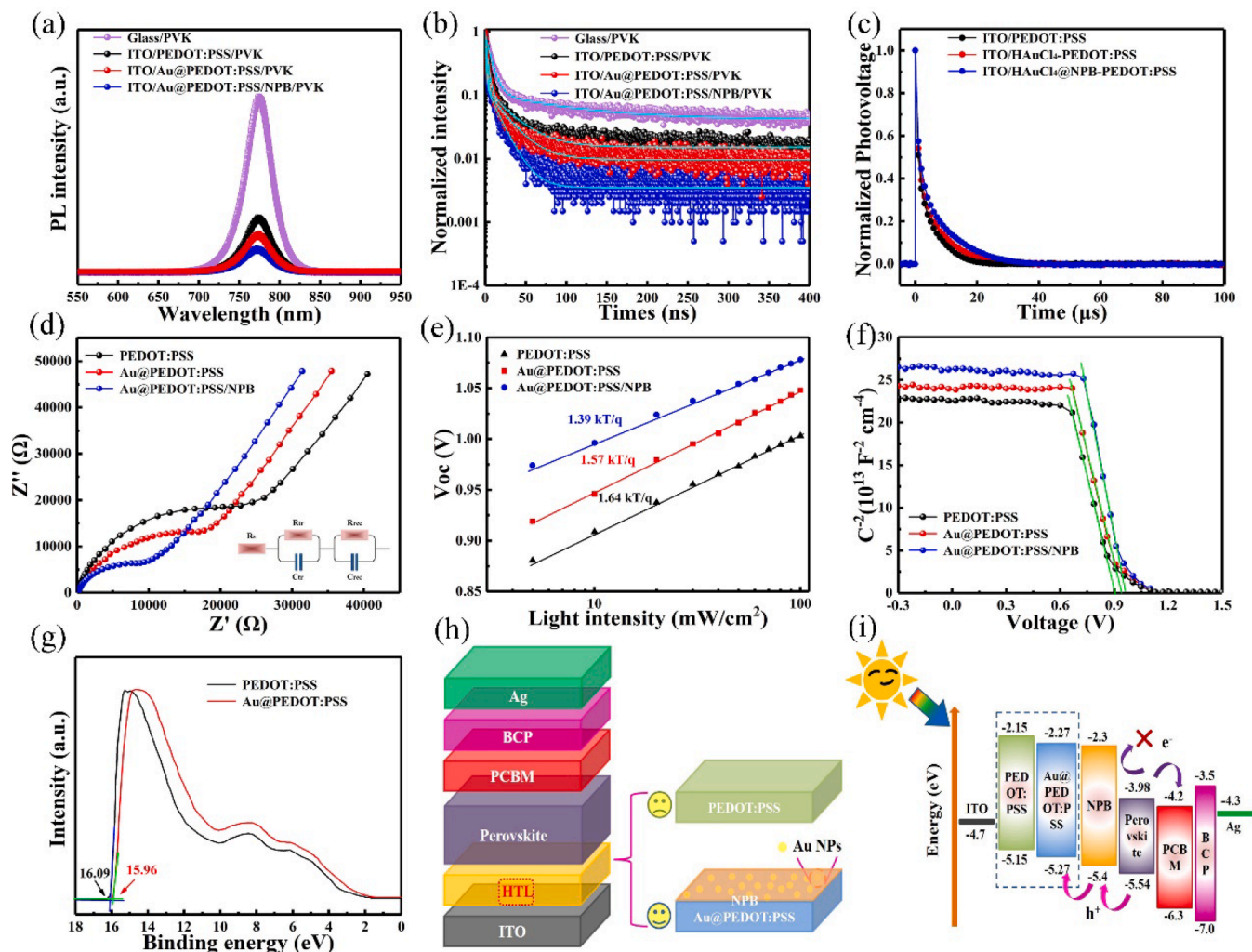


Fig. 6. (a) Steady-state PL spectra, (b) TRPL decay curves of perovskite films spin-coated on glass, pristine, Au@PEDOT:PSS and Au@PEDOT:PSS/NPB films. (c) TPV measurements of perovskite films spin-coated on pristine, Au@PEDOT:PSS and Au@PEDOT:PSS/NPB films. (d) Nyquist plots of these PSCs measured in the dark with a bias voltage of 0 V. (e) V_{oc} vs illumination intensity plots of the corresponding devices. (f) Mott-Schottky plots of the corresponding devices. (g) UPS binding energy spectra of PEDOT:PSS films doped with and without HAuCl_4 . (h) Device structure, (i) Energy level diagram of the materials used in the inverted PSCs.

Au@PEDOT:PSS and Au@PEDOT:PSS/NPB HTLs. As presented in Fig. 6c, a longer lifetime ($\tau = 9.67$ ns) can be obtained for the Au@PEDOT:PSS/NPB based sample compared with that of the Au@PEDOT:PSS ($\tau = 6.84$ ns) and pristine ($\tau = 5.63$ ns) based ones. These results indicated the co-modification of HAuCl₄ and NPB successfully promoted the effective separation of exciton and the extraction process of hole carriers. [73]

To further investigate the charge transport and recombination dynamics within the devices, electrochemical impedance spectroscopy (EIS) measurements were executed in the frequency range of 1 Hz to 10⁶ Hz under dark conditions. The Nyquist plots of the devices based on pristine, Au@PEDOT:PSS and Au@PEDOT:PSS/NPB HTLs were illustrated in Fig. 6d, where the inset showed the simulated equivalent circuit model consisting of series resistance (R_s), transfer resistance (R_{tr}) and recombination resistance (R_{rec}). These corresponding parameter values are associated with the high frequency intercept, high frequency and low frequency arc radius sizes, respectively, and the details have been summarized in Table S7. [74] For Au@PEDOT:PSS/NPB based device, a significant reduction in R_{tr} and an increase in R_{rec} can greatly facilitate charge transfer and suppress charge recombination rates.

To more intuitively investigate and analyze the charge recombination process within the devices, we have also conducted the light intensity-dependent Voc measurements, as shown in Fig. 6e. The dependence of Voc on light intensity is determined by the following relationship:

$$V_{oc} = nkT \ln(I)/q$$

Where, the slopes of Au@PEDOT:PSS and Au@PEDOT:PSS/NPB based device decreased from 1.64 kT/q to 1.57 kT/q and 1.39 kT/q, respectively, compared with that of the pristine one, indicating the successful inhibition of trap-assisted Shockley-Read-Hall (SRH) charge recombination. Mott-Schottky (M-S) plots were obtained from capacitance-voltage (C²-V) measurements and were presented in Fig. 6f to further demonstrate the variations in Voc and interfacial properties of the devices based on the pristine, Au@PEDOT:PSS and Au@PEDOT:PSS/NPB HTLs. The values of the built-in potential (V_{bi}) can be obtained through the following formula [75]:

$$1/C^2 = 2(V_{bi}-V)/q\epsilon\epsilon_0N$$

where C is the space charge capacitance, N is the charge density, V is the applied voltage, and q, ϵ , and ϵ_0 are the elementary charge, dielectric constant and vacuum permittivity, respectively. It can be found that the V_{bi} of Au@PEDOT:PSS/NPB device was 0.97 V, while the V_{bi} based on pristine and Au@PEDOT:PSS HTLs were 0.90 V and 0.94 V, respectively. We have learnt that the extended depletion region can reduce the interfacial contact barrier and promote the effective separation of charge carriers, thereby reducing the interfacial recombination.

In aggregate, such improvement in charge separation and transfer processes as testified by the above characterizations can be attributed to the high quality of both the HTLs and perovskite films, as well as the improved interfacial properties between them. Besides of these factors, it is also possible to stem from the more favorable energy band alignment of NPB with Au@PEDOT:PSS HTL and perovskite film, as well as the good p-type conductive properties of NPB. Thus, ultraviolet photoelectron spectroscopy (UPS) was then employed to determine the energy level structures of the pristine, Au@PEDOT:PSS HTLs and NPB buffer layer. As shown in Fig. 6h and Figure S17, the VBE of the pristine and Au@PEDOT:PSS films can be determined as 5.13 eV and 5.29 eV, respectively. While, the bandgap and VBE of the NPB buffer layer were calculated as 3.1 eV and 5.4 eV from the UV-vis absorption spectra and UPS spectra of NPB, respectively. Obviously, the usage of HAuCl₄ enabled the better match of modified HTL with the VBE of the NPB buffer layer and perovskite film, which is more conducive to effective charge transport and result in reduced Voc losses. [76] For more visualization, the corresponding device structure and energy level alignment diagrams of the ITO/PEDOT:PSS (Au@PEDOT:PSS)/NPB/MA_{0.85}FA_{0.15}PbI₃/PCBM/BCP/Ag system were shown in Fig. 6i and j. The introduction of the NPB buffer layer not only allow for a more

adequate and efficient extraction of the hole carriers, but also largely inhibit the direct contact between the generated Au NPs and the perovskite film, which will have a positive modulating effect on the PV performance and stability of the devices.

Reproducibility and stability are two other key factors to examine device performance. Box plots of PV parameters, including J_{sc}, Voc, FF and PCE were derived from 20 pristine, Au@PEDOT:PSS and Au@PEDOT:PSS/NPB based devices under the same measurement conditions, respectively. As shown in Fig. 7a-d, the Au@PEDOT:PSS/NPB based devices have narrower distributions of parameters compared with those of the pristine and Au@PEDOT:PSS based ones, which indicates a significant improvement in reproducibility and PV performance. In addition, steady-state PCE was also conducted at the maximum power point voltage (V_{mpp}) to present the stability of the operational output. As shown in Fig. 7e, the V_{mpp} values for the pristine, Au@PEDOT:PSS and Au@PEDOT:PSS/NPB based devices were 0.801 V, 0.823 V and 0.864 V, and the stabilized PCE values were 14.91%, 16.71% and 18.64%, respectively after continuous illumination of 200 s, which well matched with the corresponding PCE obtained from the J-V curves. The corresponding devices were also subjected to long-term stability measurements at 25 °C and 45% relative humidity (RH) for one month. The corresponding decay curves were presented in Fig. 5d. The Au@PEDOT:PSS/NPB based device maintained a slower decay rate throughout the measurements, which was able to maintain 81% of the initial PCE at the end of the test, compared with that of 66% and 74% for the pristine and Au@PEDOT:PSS based counterparts, respectively. In general, grain boundaries have been recognized to be the main channel for moisture penetration and ion migration within polycrystalline perovskites, which also determines the decomposition rate of the devices. Therefore, the improved crystalline quality of perovskite films, such as enlarged grain size, reduced grain boundaries and suppressed non-radiative defects, as well as the excellent hydrophobic properties of NPB in our case, eventually improved the structure and moisture stability of the devices.

We have also fabricated the corresponding PSCs on ITO/PEN flexible substrates under the optimal conditions described above, and the device structure schematic and J-V curves were shown in Figure S18a and b. For the champion Au@PEDOT:PSS/NPB based device, a high PCE of up to 14.04% with Voc of 0.94 V, J_{sc} of 20.56 mA cm⁻² and FF of 72.47% can be achieved under RS conditions, while a rather lower HI of 0.068 has been obtained for the device. However, the PV performance of the flexible devices is still poor compared with that of the rigid counterparts, which could be attributed to the lower light transmission of ITO/PEN compared with that of the ITO substrates, and the inferior interfacial properties between ITO/PEN and HTL. Nevertheless, our method still has merits for improving the performance of flexible and tandem devices.

3. Conclusion

In summary, an effective approach was proposed to simultaneously ameliorate the PV performance and stability of the devices through co-modifying the PEDOT:PSS HTLs with HAuCl₄ and NPB. Wherein, the doping of inorganic HAuCl₄ into PEDOT:PSS aqueous solution can lead to the phase segregation of the conducting PEDOT and insulating PSS⁻ parts of the PEDOT:PSS conjugated polymer system due to the redox reaction between PEDOT:PSS and HAuCl₄, which contributes to the formation of PSSH, allowing the PEDOT chains to form a liner or extended coil structure, which generates more charge carriers and increases the electrical conductivity of the pristine PEDOT:PSS film. Moreover, the reduced Au NPs can also elevate the harvesting efficiency of solar radiation and increase the light scattering ability due to the LSPR effect. Nevertheless, if the Au NPs come into direct contact with the perovskite film, it will impair the effective separation of excitons, which will greatly hinder the further improvement of device performance. To address this problem, we further improved this deficiency by using organic NPB, a p-type material with good electrical conductivity, to

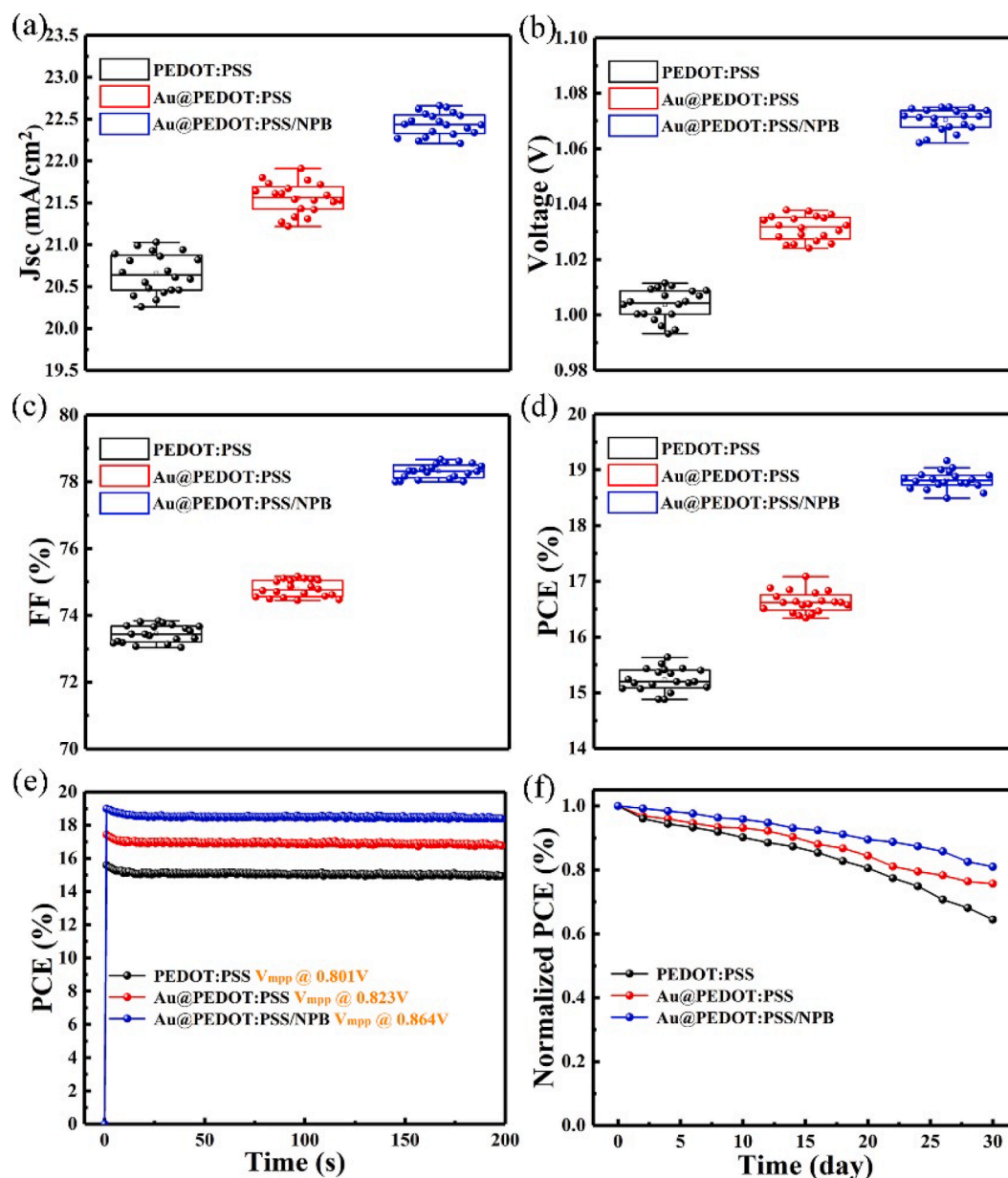


Fig. 7. Standard box plot of (a) J_{sc} , (b) V_{oc} , (c) FF, (d) PCE for pristine, Au@PEDOT:PSS and Au@PEDOT:PSS/NPB based devices, respectively. (e) Steady-state PCE output profiles for the best performance of pristine, Au@PEDOT:PSS and Au@PEDOT:PSS/NPB based PSCs. (f) Long-term stability of unencapsulated pristine, Au@PEDOT:PSS and Au@PEDOT:PSS/NPB based devices measured at ambient air conditions 25 °C, 20% < RH < 50%.

serve as a buffer layer deposited on Au@PEDOT:PSS films. Since the suitable VBM with respect to perovskite film and Au@PEDOT:PSS HTL, better hydrophobicity, stronger passivation effect and excellent stability of the NPB buffer layer, Au@PEDOT:PSS/NPB based device can achieve a high PCE of 19.20% on rigid the substrates and 14.04% on flexible substrates. With the improvement of the crystal quality of polycrystalline perovskites and interfacial properties, especially for the interfacial charge extraction properties and the effective passivation of defects within the device, the hysteresis behavior of the device is greatly suppressed and the long-term stability is well regulated. Our work demonstrates that the HAuCl₄ and NPB co-modification method shows great potential for achieving high-performance and stable p-i-n planar PV devices on both rigid and flexible substrates due to the synergistic effect.

Declaration of Competing Interest

The authors declare that they have no known competing financial interests or personal relationships that could have appeared to influence the work reported in this paper.

Acknowledgements

The authors would like to acknowledge financial support for this work from National Nature Science Foundation of China (Grant Nos. 22075101, 61775081, 61904066, 11904127, 61475063, and 22078124), Program for the development of Science and Technology of Jilin province (Item No. 20200801032GH), Program for the creative and innovative talents of Jilin Province (Item No. 2020028), Science and technology research project of Jilin Provincial Department of Education (Item No. JJKH20210440KJ).

Appendix A. Supplementary data

Supplementary data to this article can be found online at <https://doi.org/10.1016/j.cej.2021.134358>.

References

- [1] Best Research-Cell Efficiencies [Online]. NREL, <https://www.nrel.gov/pv/assets/pdfs/cell-pv-eff-emergingpv.20200919.pdf> (accessed 25 September 2020).
- [2] D. Bi, C. Yi, J. Luo, J.-D. Décoppet, F. Zhang, S.M. Zakeeruddin, X. Li, A. Hagfeldt, M. Grätzel, *Nat. Energy*. 1 (2016) 16142.
- [3] X. Zheng, B. Chen, J. Dai, Y. Fang, Y. Bai, Y. Lin, H. Wei, X. Zeng, J. Huang, *Nat. Energy*. 2 (2017) 17102.
- [4] Y. Deng, X. Zheng, Y. Bai, Q. Wang, J. Zhao, J. Huang, *Nat. Energy*. 3 (2018) 560–566.
- [5] S. Yang, J. Dai, Z. Yu, Y. Shao, Y. Zhou, X. Xiao, X. Zeng, J. Huang, *J. Am. Chem. Soc.* 141 (2019) 5781–5787.
- [6] C. Zuo, L. Ding, *Adv. Energy Mater.* 7 (2017) 1601193.
- [7] C. Cho, K.L. Wallace, P. Tzeng, J.-H. Hsu, C. Yu, J.C. Grunlan, *Adv. Energy Mater.* 6 (2016) 1502168.
- [8] C. Xie, P. You, Z. Liu, L. Li, F. Yan, *Light, Sci. Appl.* 6 (2017), e17023.
- [9] Y. Hou, H. Zhang, W. Chen, S. Chen, C.O.R. Quiroz, H. Azimi, A. Osvet, G.J. Matt, E. Zeira, J. Seuring, N. Kausch-Busies, W. Lövenich, C.J. Brabec, *Adv. Energy Mater.* 5 (2015) 1500543.
- [10] Y. Shao, Z. Xiao, C. Bi, Y. Yuan, J. Huang, *Nat. Commun.* 5 (2014) 5784.
- [11] H.-H. Fang, F. Wang, S. Adjokate, N. Zhao, J. Even, M.A. Loi, *Light, Sci. Appl.* 5 (2016), e16056.
- [12] W. Li, W. Zhang, S. Van Reenen, R.J. Sutton, J. Fan, A.A. Haghighirad, M. B. Johnston, L. Wang, H.J. Snaith, *Energy Environ. Sci.* 9 (2016) 490–498.
- [13] A. Buin, P. Pietsch, J. Xu, O. Voznyy, A.H. Ip, R. Comin, E.H. Sargent, *Nano Lett.* 14 (2014) 6281–6286.
- [14] X. Xiao, C. Bao, Y. Fang, J. Dai, B.R. Ecker, C. Wang, Y. Lin, S. Tang, Y. Liu, Y. Deng, X. Zheng, Y. Gao, X.C. Zeng, J. Huang, *Adv. Mater.* 30 (2018) 1705176.
- [15] H.-L. Yip, A.K.-Y. Jen, *Energy Environ. Sci.* 5 (2012) 5994–6011.
- [16] H. Elbohy, B. Bahrami, S. Mabrouk, K.M. Reza, A. Gurung, R. Pathak, M. Liang, Q. Qiao, K. Zhu, *Adv. Funct. Mater.* 29 (2018) 1806740.
- [17] J.P. Thomas, L. Zhao, D. McGillivray, K.T. Leung, *J. Mater. Chem. A* 2 (2014) 2383–2389.
- [18] J.-T.-W. Wang, Z. Wang, S. Pathak, W. Zhang, D.W. deQuilettes, F. Wisnivesky-Rocca-Rivarola, J. Huang, P.K. Nayak, J.B. Patel, H.A.M. Yusuf, Y. Vaynzof, R. Zhu, I. Ramirez, J. Zhang, C. Ducati, C. Grovenor, M.B. Johnston, D.S. Ginger, R. J. Nicholas, H.J. Snaith, *Energy Environ. Sci.* 9 (2016) 2892–2901.
- [19] B. Anothumakkool, R. Soni, S.N. Bhange, S. Kurungot, *Energy Environ. Sci.* 8 (2015) 1339–1347.
- [20] I. Lee, G.W. Kim, M. Yang, T.-S. Kim, *ACS Appl. Mater. Interfaces* 8 (2015) 302–310.
- [21] S. Kim, B. Sanyoto, W.-T. Park, S. Kim, S. Mandal, J.-C. Lim, Y.-Y. Noh, J.-H. Kim, *Adv. Mater.* 28 (2016) 10149–10154.
- [22] Z. Li, W. Meng, J. Tong, C. Zhao, F. Qin, F. Jiang, S. Xiong, S. Zeng, L. Xu, B. Hu, Y. Zhou, *Sol. Energy Mater. Sol. Cells* 137 (2015) 311–318.
- [23] C. Zuo, D. Vak, D. Angmo, L. Ding, M. Gao, *Nano Energy*. 46 (2018) 185–192.
- [24] D. Zhao, M. Sexton, H.-Y. Park, G. Baure, J.C. Nino, F. So, *Adv. Energy Mater.* 5 (2015) 1401855.
- [25] M. Wang, H. Wang, W. Li, X. Hu, K. Sun, Z. Zang, *J. Mater. Chem. A* 7 (2019) 26421–26428.
- [26] F. Hou, Z. Su, F. Jin, X. Yan, L. Wang, H. Zhao, J. Zhu, B. Chu, L. Li, *Nanoscale* 7 (2015) 9427–9432.
- [27] W. Yan, S. Ye, Y. Li, W. Sun, H. Rao, Z. Liu, Z. Bian, C. Huang, *Adv. Energy Mater.* 6 (2016) 1600474.
- [28] P. Qin, T. Wu, Z. Wang, L. Xiao, L. Ma, F. Ye, L. Xiong, X. Chen, H. Li, X. Yu, G. Fang, *Adv. Funct. Mater.* 30 (2020) 1908408.
- [29] J.H. Heo, H.J. Han, D. Kim, T.K. Ahn, S.H. Im, *Energy Environ. Sci.* 8 (2015) 1602–1608.
- [30] Z. Zhu, Q. Xue, H. He, K. Jiang, Z. Hu, Y. Bai, T. Zhang, S. Xiao, K. Gundogdu, B. R. Gautam, H. Ade, F. Huang, K.S. Wong, H.-L. Yip, S. Yang, H. Yan, *Adv. Sci.* 3 (2016) 1500353.
- [31] H.B. Jeon, P.V. Tsalu, J.W. Ha, *Sci Rep.* 9 (2019) 13635.
- [32] C.-C. Chang, H.-L. Wu, C.-H. Kuo, M.H. Huang, *Chem. Mater.* 20 (2008) 7570–7574.
- [33] T. Ye, S. Ma, X. Jiang, L. Wei, C. Vijila, S. Ramakrishna, *Adv. Funct. Mater.* 27 (2017) 1606545.
- [34] S.S. Kumar, C.S. Kumar, J. Mathiyarasu, K.L. Phani, *Langmuir*. 23 (2007) 3401–3408.
- [35] Y. Zhao, H. Su, Q. Liu, L. Zhang, M. Lv, C. Jiao, P. Chen, D. Liu, D. He, *ACS Omega*. 5 (2020) 7545–7554.
- [36] H. Hao, L. Wang, X. Ma, K. Cao, H. Yu, M. Wang, W. Gu, R. Zhu, M.S. Anwar, S. Chen, W. Huang, *Sol. RRL*. 2 (2018) 1800061.
- [37] L. Hu, M. Li, K. Yang, Z. Xiong, B. Yang, M. Wang, X. Tang, Z. Zang, X. Liu, B. Li, Z. Xiao, S. Lu, H. Gong, J. Ouyang, K. Sun, *J. Mater. Chem. A* 6 (2018) 16583–16589.
- [38] J.W. Jo, M.-S. Seo, M. Park, J.-Y. Kim, J.S. Park, I.K. Han, H. Ahn, J.W. Jung, B.-H. Sohn, M.J. Ko, H.J. Son, *Adv. Funct. Mater.* 26 (2016) 4464–4471.
- [39] Y. Xia, J. Ouyang, *J. Mater. Chem.* 21 (2011) 4927–4936.
- [40] H. Yu, Z. Wu, X. Huang, S. Shi, Y. Li, *Org. Electron.* 62 (2018) 121–132.
- [41] Y. Huang, L. Ma, M. Hou, J. Li, Z. Xie, Z. Zhang, *Sci Rep.* 6 (2016) 30011.
- [42] Z. Fan, P. Li, D. Du, J. Ouyang, *Adv. Energy Mater.* 7 (2017) 1602116.
- [43] J. Huang, P.F. Miller, J.S. Wilson, A.J. de Mello, J.C. de Mello, D.D.C. Bradley, *Adv. Funct. Mater.* 15 (2005) 290–296.
- [44] J. Luo, D. Billep, T. Waechtler, T. Otto, M. Toader, O. Gordan, E. Sheremet, J. Martin, M. Hietschold, D.R.T. Zahnd, T. Gessner, *J. Mater. Chem. A* 1 (2013) 7576–7583.
- [45] W.W. Chiu, J. Travas-Sejdic, R.P. Cooney, G.A. Bowmaker, *J. Raman Spectrosc.* 37 (2006) 1354–1361.
- [46] S. Vempati, Y. Ertas, A. Celebioglu, T. Uyar, *Appl. Surf. Sci.* 419 (2017) 770–777.
- [47] Z. Wu, Z. Yu, H. Yu, X. Huang, M. Chen, *J. Mater. Sci.-Mater. Electron.* 29 (2018) 6607–6618.
- [48] O. Bubnova, Z.U. Khan, H. Wang, S. Braun, D.R. Evans, M. Fabretto, P. Hojati-Talemi, D. Dagnelund, J.-B. Arlin, Y.H. Geerts, S. Desbief, D.W. Breiby, J. W. Andreasen, R. Lazzaroni, W.M. Chen, I. Zozoulenko, M. Fahlman, P.J. Murphy, M. Berggren, X. Crispin, *Nat. Mater.* 13 (2014) 190–194.
- [49] Q. Xue, M. Liu, Z. Li, L. Yan, Z. Hu, J. Zhou, W. Li, X.-F. Jiang, B. Xu, F. Huang, Y. Li, H.-L. Yip, Y. Cao, *Adv. Funct. Mater.* 28 (2018) 1707444.
- [50] J. Dong, G. Portale, *Adv. Mater. Interfaces*. 7 (2020) 2000641.
- [51] S.R. Pathipati, M.N. Shah, X. Pan, *Sol. Energy*. 197 (2020) 363–370.
- [52] Y. Yang, L. Yang, S. Feng, *Mater. Today Adv.* 6 (2020), 100068.
- [53] P.S. Chandrasekhar, A. Dubey, K.M. Reza, M.D.N. Hasan, B. Bahrami, V. K. Komarala, J.D. Hoefelmeyer, Q. He, F. Wu, H. Qiao, W.-H. Zhang, Q. Qiao, *Sustain. Energy Fuels*. 2 (2018) 2260–2267.
- [54] S. Park, H. Lee, J. Lee, Y. Lee, Y. Yi, *Org. Electron.* 15 (2014) 3298–3305.
- [55] P. Huang, Y. Liu, K. Zhang, L. Yuan, D. Li, G. Hou, B. Dong, Y. Zhou, B. Song, Y. Li, *J. Mater. Chem. A* 5 (2017) 24275–24281.
- [56] Y. Sun, Y. Cao, L. Wang, X. Mu, Q. Zhao, R. Si, X. Zhu, S. Chen, B. Zhang, D. Chen, Y. Wan, *Nat. Commun.* 11 (2020) 4600.
- [57] Y. Sun, Z. Pang, Y. Quan, D. Han, X. Zhang, X. Ge, F. Wang, Y. Sun, J. Yang, *L. Yang, Chem. Eng. J.* 413 (2021), 127387.
- [58] U. Lang, E. Müller, N. Naujoks, J. Dual, *Adv. Funct. Mater.* 19 (2009) 1215–1220.
- [59] J. Ouyang, *Displays* 34 (2013) 423–436.
- [60] H. Hu, M. Singh, X. Wan, J. Tang, C.-W. Chu, G. Li, *J. Mater. Chem. A* 8 (2020) 1578–1603.
- [61] Y. Sun, S. Yang, Z. Pang, Y. Quan, R. Song, Y. Chen, W. Qi, Y. Gao, F. Wang, X. Zhang, Y. Sun, J. Yang, L. Yang, F. Rosei, *ACS Appl. Mater. Interfaces* 13 (2021) 10822–10836.
- [62] Q. Jiang, Z. Chu, P. Wang, X. Yang, H. Liu, Y. Wang, Z. Yin, J. Wu, X. Zhang, J. You, *Adv. Mater.* 29 (2017) 1703852.
- [63] W.-Q. Wu, Z. Yang, P.N. Rudd, Y. Shao, X. Dai, H. Wei, J. Zhao, Y. Fang, Q. Wang, Y. Liu, Y. Deng, X. Xiao, Y. Feng, J. Huang, *Sci. Adv.* 5 (2019) eaav8925.
- [64] X. Li, W. Li, Y. Yang, X. Lai, Q. Su, D. Wu, G. Li, K. Wang, S. Chen, X. Sun, A.K. K. Kyaw, *Sol. RRL* 3 (2019) 1900029.
- [65] H. Lu, A. Krishna, S.M. Zakeeruddin, M. Grätzel, *iScience* 23 (2020) 101359.
- [66] J.M. Ball, A. Petrozza, *Nat. Energy*. 1 (2016) 16149.
- [67] Q. Wang, Y. Shao, Q. Dong, Z. Xiao, Y. Yuan, J. Huang, *Energy Environ. Sci.* 7 (2014) 2359–2365.
- [68] Y. Wang, Z. Zhang, M. Tao, Y. Lan, M. Li, Y. Tian, Y. Song, *Nanoscale* 12 (2020) 18563–18575.
- [69] M.S. Alva, P.W.M. Blom, G.-J.A.H. Wetzelaer, *Nat. Commun.* 11 (2020) 4023.
- [70] H. Wang, F. Yang, Y. Xiang, S. Ye, X. Peng, J. Song, J. Qu, W.-Y. Wong, *J. Mater. Chem. A* 7 (2019) 24191–24198.
- [71] F. Wang, M. Yang, Y. Zhang, L. Yang, L. Fan, S. Lv, X. Liu, D. Han, J. Yang, *Adv. Sci.* 6 (2019) 1801170.
- [72] N.J. Jeon, J.H. Noh, W.S. Yang, Y.C. Kim, S. Ryu, J. Seo, S.I. Seok, *Nature* 517 (2015) 476–480.
- [73] S. Yue, K. Liu, R. Xu, M. Li, M. Azam, K. Ren, J. Liu, Y. Sun, Z. Wang, D. Cao, X. Yan, S. Qu, Y. Lei, Z. Wang, *Energy Environ. Sci.* 10 (2017) 2570–2578.
- [74] H.-S. Kim, I. Mora-Sero, V. Gonzalez-Pedro, F. Fabregat-Santiago, E.J. Juarez-Perez, N.-G. Park, J. Bisquert, *Nat. Commun.* 4 (2013) 2242.
- [75] A. Guerrero, E.J. Juarez-Perez, J. Bisquert, I. Mora-Sero, G. Garcia-Belmonte, *Appl. Phys. Lett.* 105 (2014), 133902.
- [76] P. Chen, Y. Bai, S. Wang, M. Lyu, J.-H. Yun, L. Wang, *Adv. Funct. Mater.* 28 (2018) 1706923.